Toward efficient and robust computation of energy release rate and mode mix for delamination

Frans van der Meer, Lambertus J Sluys, Nicolas Moës

Toward efficient and robust computation of energy release rate and mode mix for delamination

F.P. van der Meer [a,*], L.J. Sluys [a], N. Moës [b]

[a] Delft University of Technology, Faculty of Civil Engineering and Geosciences, PO Box 5048, 2600 GA Delft, The Netherlands
[b] Ecole Centrale de Nantes, GeM Institute, UMR CNRS 6183, 1 Rue de la Noë, 44321 Nantes, France

Different methods for computing energy release rates for delamination are assessed with emphasis on their performance with large elements and irregular meshes. The jump in stress and strain that appears at the crack front with shell kinematics is used to compute the energy release rate in a simple manner via the jump in Eshelby tensor, without the mesh requirements that are associated with the virtual crack closure technique. The robustness of the results is examined for different kinematic formulations. For mode partitioning, another method that also makes use of the jump in stress [15], is modified for better performance with large elements. In this manner, the proposed method connects to existing concepts for characterization of fracture toughness based on linear elastic fracture mechanics. However, by presenting a size effect in the mode mix predicted with a cohesive method, it is emphasized that the validity of these concepts is questionable.

1. Introduction

It is a central thesis of fracture mechanics that a crack grows when the energy that will be released upon crack growth, the energy release rate G, is greater than the amount of energy that is required to form new crack surface, the fracture toughness G_c [1]. The criterion for crack growth is written as:

$$G \geqslant G_c \tag{1}$$

Hence, energy release rate computation is of interest for simple assessment of criticality of a given crack under given loads, as well as for more advanced progressive cracking analysis. The energy release rate can be computed with stress intensity factors, [2], with the J-integral [3] or with the virtual crack closure technique (VCCT) [4,5]. The VCCT is often applied to delamination problems, particularly for cases where one is interested in the energy release rate for a given front location. In the VCCT, the energy release rate is obtained in a relatively simple post-processing step, but it is required that the crack front coincides with element boundaries and that the mesh is fine and regularly spaced around the crack front. These requirements make the method laborious, particularly for progressive failure analysis. For this reason, cohesive methods are preferred for progressive failure simulations [6–10]. However, cohesive methods have a restriction on the mesh size, which causes their applicability to be limited to relatively small samples. The element size is namely required to be several times smaller than the length of the cohesive zone, which is for most laminates and load cases of the order of 1 mm.

In a fracture mechanics approach to delamination, it is important to account for the fact that the interfacial fracture toughness of laminates is not a material constant but rather a function of the opening mode [11,12]. For evaluation of criterion (1), it is therefore necessary to compute not only the energy release rate G but also a measure for the current opening mode which can be related to measurements of the fracture toughness G_c under different conditions. In cohesive methods and the VCCT, this is done by partitioning G into three contributions that are related to the fundamental modes:

$$G = G_I + G_{II} + G_{III} \tag{2}$$

and postulating that G_c is a function of the ratios between those three values:

$$G_c = G_c\left(\frac{G_I}{G}, \frac{G_{II}}{G}\right) \tag{3}$$

It should be noted that the partitioning in pure mode release rates in Eq. (2) is theoretically not valid for cracks on a bimaterial interface [13]. In the VCCT this is reflected in non-convergence of the pure mode release rates [14]. This can be eliminated by assuming that cracking occurs in a thin homogeneous interphase layer [14], but this comes at the cost of having to use very small finite

* Corresponding author. Tel.: +31 (0)15 278 5918; fax: +31 (0)15 278 5767.
E-mail addresses: f.p.vandermeer@tudelft.nl (F.P. van der Meer), l.j.sluys@tudelft.nl (L.J. Sluys), nicolas.moes@ec-nantes.fr (N. Moës).

Nomenclature

A, B, C	different subdomains of a partially delaminated beam/shell
A, I	cross-section and second moment of inertia of a beam
c	crack length
c_1, c_2	auxiliary coefficients (Davidson's method)
D_{ij}	laminate bending stiffness matrix
E	Young's modulus
F_i	distributed force vector between sublaminates (Zou's method)
F_m, F_e	point loads in mixed-mode bending test
G	energy release rate
G_I, G_{II}, G_{III}	pure mode components of energy release rate
$\overline{G}$	reference energy release rate (test-dependent, for normalization)
G_c	fracture toughness
h, h_B, h_C	thickness
H_{ij}	laminate transverse shear stiffness matrix
K_n, K_s	Elastic rotation spring stiffness
K_I, K_{II}	stress intensity factors
L	specimen length
n, s, z	coordinates aligned with the crack front
$\mathbf{n}$	normal vector to the crack front
$\mathbf{N}, N_{ij}$	shell force tensor
N_c, M_c	equivalent force and moment (Davidson's method)
$\mathbf{M}, M_{ij}$	shell bending moment tensor
$\mathbf{P}, P_{ij}$	Eshelby tensor
$\mathbf{Q}, Q_i$	shell transverse shear force vector
T_i	distributed bending moment vector
$\mathbf{u}, u_i$	displacement vector
$\mathbf{u}^0, u_i^0$	displacement vector at the shell mid-plane
x, y, z	global coordinates
Δx	element length
α	Timoshenko's shape coefficient
β^{in}	global mode ratio from beam theory
β^{out}	mode ratio computed from local quantities
$\boldsymbol{\gamma}, \gamma_{iz}$	shell transverse shear deformation vector
Γ, Ω	auxiliary coefficients (Davidson's method)
δ_{ij}	Kronecker delta
ε_{ij}	strain tensor
κ	beam curvature
λ	slenderness coefficient
μ	shear modulus
σ_{ij}	stress tensor
$\boldsymbol{\phi}, \phi_i$	shell rotation vector

Abbreviations

6ECT	six-point edge cracked torsion
DCB	double cantilever beam
LEFM	linear elastic fracture mechanics
MITC	mixed interpolation of tensorial components
MMB	mixed mode bending
UDCB	unsymmetric double cantilever beam
VCCT	virtual crack closure technique

elements. Zou et al. [15–17] have introduced an alternate technique in which the oscillations are removed without the assumptions of an interphase layer.

But even when partitioning of the energy release rates is possible, the assumption that the fracture toughness depends on the ratios between the pure release rates is debatable. In Eq. (3) a separation of scales is assumed between the length of the fracture process zone and the fluctuations in the surrounding stress and strain fields. Only in that case, the stress field that drives the micromechanical fracture process can be completely characterized by the stress intensity factors K_I, K_{II} and K_{III} and hence also by pure mode energy release rates G_I, G_{II} and G_{III}. This condition is not generally true for laminates, where the fracture process zone is often larger than the ply thickness [6]. Indeed, Davidson et al. have shown that a fracture mechanics characterization of the mode mix does not in all cases give the best estimate of G_c [18,19]. Furthermore, it should be noted that the fracture toughness may also depend on ply thickness [20] and relative fiber orientation [21]. The problem how to characterize the fracture toughness will not be solved in this paper, but the fact that this is an open question will be highlighted with new numerical results.

In recent work [22], we have proposed a new method for progressive delamination analysis. This method uses level sets to allow for an implicit representation of the moving crack front through the domain without restrictive mesh requirements. The energy release rate is computed along the front with the jump in Eshelby tensor. It is shown that, after making the right kinematic assumptions, there is no need to compute the singular field around the crack tip in order to get an accurate value for the energy release rate.

In the current paper the proposed method to compute the energy release rate is investigated in more detail. The primary motivation for this study comes from the development of the mentioned progressive delamination model, but it is acknowledged that energy release rate computation with a fixed crack location is also of interest. Therefore the current paper deals only with cases with a given crack location that coincides with element boundaries. The aim is to find a method for energy release computation which gives accurate values for coarse and possibly irregular meshes as well as an indication of the mode mix.

In the two sections that follow this introduction, two different topics are investigated. Firstly, the performance of different discretization types is examined in terms of accuracy of the computed total energy release rate. The main questions are how the connection between the cracked and the uncracked part is best represented and whether solid elements or beam/shell elements are to be preferred. Secondly, the topic of mode mixity is addressed. For this purpose, the method developed by Zou et al. [15–17] is investigated as a method that not only gives the total energy release rate but also allows for partitioning of this number into three pure mode contributions. The accuracy of this method in predicting pure mode energy release rates with large elements is evaluated with mesh-refinement studies on mixed-mode cases. An improved formulation is proposed in this paper. In the course of this investigation, an inconsistency is demonstrated in different accepted approaches to energy release rate partitioning.

2. Total energy release rate

Let the domain of a partially delaminated plate be subdivided into three regions A, B and C, such that A represents the uncracked part, and B and C the bottom and top arms of the cracked part, respectively (see Fig. 1). When the kinematic assumptions of shell theory are applied, the interface that separates A from B and C is a configurational interface over which a jump in strain occurs. The jump in strain is the shell equivalent of the singularity that is known to exist around the crack tip in the continuum

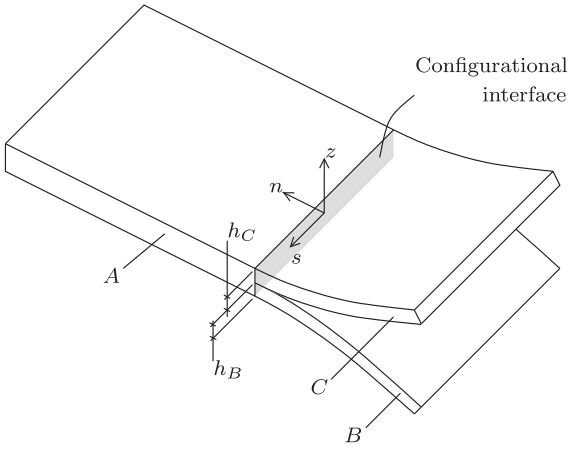

Fig. 1. Definitions for a partially delaminated plate.

three-dimensional solution. Just as the intensity of the stress singularity in the continuum solution gives information on the energy release rate, so does the magnitude of the jump in elastic energy in the shell solution. The energy that will be released when the configurational interface moves (i.e., when the crack grows) with unit velocity can be expressed as a function of the location along the crack front as [22]:

$$G(s) = \int_{-h_B}^{h_C} \mathbf{n} \cdot [\![\mathbf{P}]\!] \cdot \mathbf{n}\, dz \tag{4}$$

where $\mathbf{n}$ is the normal unit vector to the configurational interface (see Fig. 1) and $[\![\mathbf{P}]\!]$ is the jump in Eshelby tensor, defined as

$$[\![\mathbf{P}]\!] = \mathbf{P}|_{n=0^+} - \mathbf{P}|_{n=0^-} \tag{5}$$

with

$$P_{ij} = \frac{1}{2}\varepsilon_{kl}\sigma_{kl}\delta_{ij} - u_{k,i}\sigma_{kj} \tag{6}$$

In Eq. (6), ε_{kl} is the strain tensor, σ_{kl} is the stress tensor, $u_{k,i}$ is the gradient of the displacement vector, δ_{ij} is the Kronecker delta, and the Einstein convention is used to indicate summation over repeated indices $k,l \in [x,y,z]$. In shear deformable shell analysis, strains and stresses are decomposed into mid-plane displacement gradients $\nabla\mathbf{u}^0$, curvatures $\nabla\boldsymbol{\phi}$, transverse strains $\boldsymbol{\gamma}$, and generalized forces $\mathbf{N}$, moments $\mathbf{M}$ and shear forces $\mathbf{Q}$. The through-thickness integration of Eq. (4) can then be performed *a priori* for each of the parts *A*, *B* and *C* to give

$$\int_h \mathbf{n}\cdot\mathbf{P}\cdot\mathbf{n}\, dz = \frac{1}{2}\left(u^0_{i,j}N_{ij} + \phi_{i,j}M_{ij} + \gamma_{iz}Q_i\right) - \left(u^0_{i,n}N_{ni} + \phi_{i,n}M_{ni} + u_{z,n}Q_n\right) \tag{7}$$

with summation over $i,j \in [n,s]$.

2.1. Representation of the uncracked part: three different models

One question that needs to be answered is how the domain *A* should be discretized to obtain an efficient but accurate description of the partially cracked shell. The most efficient strategy would be to use a single layer of elements through the thickness. However, better results may be obtained when two layers of elements from the cracked part are continued in the uncracked part. Ousset [23] termed the different approaches "Model 2" and "Model 1", respectively (see Fig. 2), and showed that locking near the free edge in Model 2 may cause a disturbance in the energy release rate profile. A drawback of Model 1 seems to be that a small-scale phenomenon is introduced in the solution even for very simple cases. To illustrate this, stress fields from a double cantilever beam with the kinematic assumptions of Model 1 and Model 2 are schematically represented in Fig. 3. In both cases there is a jump in strain and stress over the configurational interface, but in Model 1 the discontuity appears in σ_{xx} and in Model 2 in σ_{xz}. What is pointed out here is that in Model 1 there are stress gradients in length direction that occur over a small region. These may harm the accuracy in energy release computation when large elements are used. While in Model 2 the stress can be captured perfectly well with very large elements.

One strategy to remove locking near the free edge as well as the small-scale stress variations is to lump the deformation of the undeformed part on the configurational interface. This can be done by using one layer of elements in the uncracked part, while relaxing the stiff rotation connection between the three parts with an elastic spring: Model 3.

2.2. Model 3 formulation

In order to get deformation of the uncracked part only for opposite curvature of the arms, the rotation spring is placed between the arms *B* and *C*, while the rotation of uncracked part *A* is tied rigidly to the weighted average of the two rotations as:

$$\boldsymbol{\phi}_A = \frac{h_B\boldsymbol{\phi}_B + h_C\boldsymbol{\phi}_C}{h_B + h_C} \tag{8}$$

where $\boldsymbol{\phi}_A$, $\boldsymbol{\phi}_B$ and $\boldsymbol{\phi}_C$ are the rotations of the three parts where they meet at $n = 0$. The distributed moments T_n and T_s acting on arms *B* and *C* from the rotation spring are related to the jump in rotations via a linear constitutive law with two stiffness parameters:

$$\begin{Bmatrix} T^B_n \\ T^B_s \end{Bmatrix} = -\begin{Bmatrix} T^C_n \\ T^C_s \end{Bmatrix} = \begin{bmatrix} K_n & 0 \\ 0 & K_s \end{bmatrix} \cdot \begin{Bmatrix} \phi^B_n - \phi^C_n \\ \phi^B_s - \phi^C_s \end{Bmatrix} \tag{9}$$

The first parameter, K_n, can be related to the rotation stiffness of a beam on elastic foundation. In finite element analysis of such system, for typical laminate properties the elastic foundation part (cf. Kanninen [24]) has been found to be smaller than the rotation due to shear deformation. Therefore the system is simplified to a semi-infinite shear deformable beam on stiff support, for which the following stiffness is found analytically:

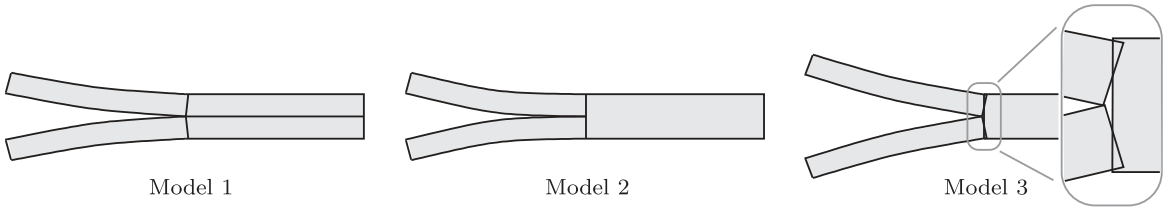

Fig. 2. Three different representations of a partially delaminated beam.

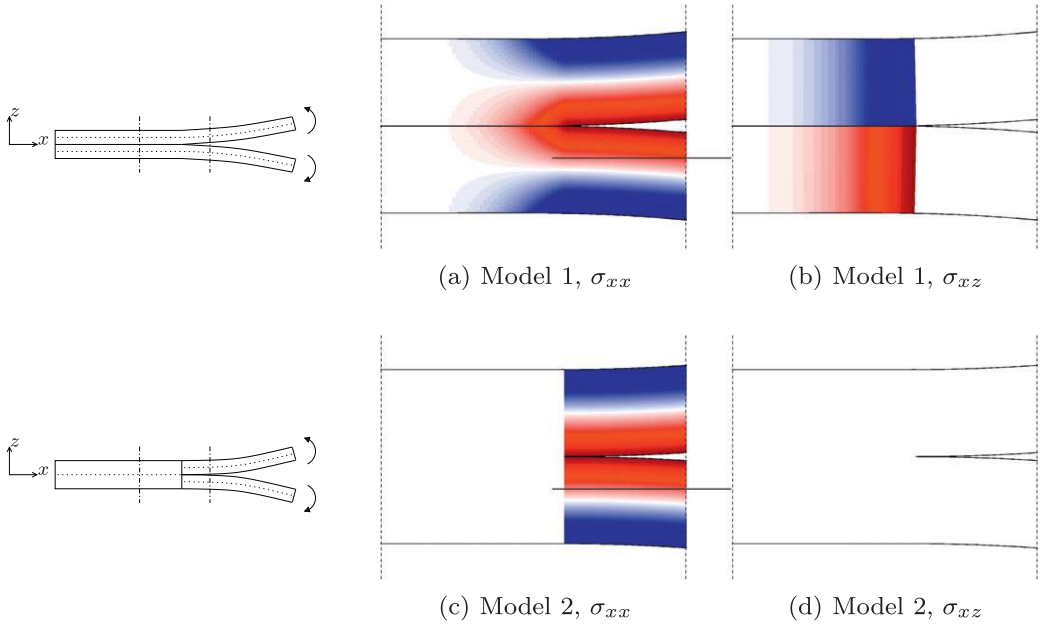

(a) Model 1, σ_{xx} (b) Model 1, σ_{xz}

(c) Model 2, σ_{xx} (d) Model 2, σ_{xz}

Fig. 3. Stress field near the sharp crack tip using either one or two layers of elements for the uncracked part.

$$\frac{M_{\text{end}}}{\phi_{\text{end}}} = \sqrt{\alpha\mu AEI} \tag{10}$$

where α is Timoshenko's shape coefficient, μ is the shear modulus, A the beam cross-section, E the Young's modulus and I the beam's second moment of inertia. For plane strain conditions perpendicular the front, this can be related to laminate stiffness quantities to get the stiffness for the distributed moment along the front. After summation of the compliance related to the two arms B and C, the relation for K_n becomes:

$$K_n = \frac{1}{\left(D^B_{nn}\widetilde{H}^B_{nn}\right)^{-1/2} + \left(D^C_{nn}\widetilde{H}^C_{nn}\right)^{-1/2}} \tag{11}$$

where D_{nn} and $\widetilde{H}_{nn}$ are entries from the bending and shear stiffness matrices from shear deformable laminate theory (notations from [25]) rotated into the $\{n,s\}$-frame aligned with the front.

The second stiffness parameter, K_s, can be set to 0. This does not lead to any spurious mechanism since global rotation of the arms around the normal to the configurational interface is prevented by the still-constrained displacements.

2.3. Numerical example: DCB

To investigate the behavior of the different models, the energy release rate along the front in a double cantilever beam (DCB) test is analyzed following Davidson [26]. For different layups and geometries, the results that have been obtained compare well to those reported by Davidson [26]. But the main emphasis here is on performance with large elements. Therefore results are presented only for one specimen (crack length/beam width = 1) with an isotropic material while the element size is varied. Simulations are performed with MITC9 shell elements (see Appendix A for more information on the elements used in this paper).

Results for the energy release rate distribution along the front are shown for the different models in Fig. 4. Results are normalized with respect to the energy release rate from the plane strain beam solution, where the shear deformation of the uncracked solution is taken into account according to Eq. (10). The results converge to a unique solution with all three methods, apart from the spurious small scale phenomenon that is observed near the free edge in Model 2. This is a similar locking as the one that has been observed by Ousset [23]. This phenomenon is indeed effectively removed by applying the rotation spring from Model 3. In fact, any low value for K_s is efficient in removing the locking effect, while the chosen value for K_n leads to the better match with the Model 1 results in the center of the specimen ($s = 0$). The maximum value at the center of the specimen is higher for Model 2. This is due to the increased stiffness of the uncracked part of Model 2 which in combination with a prescribed displacement leads to a higher energy release rate. For constant bending without shear load, the values from all models converge to the same value. Even though the jump in stress and strain are of different nature for Model 1 on the one hand and Models 2 and 3 on the other (see Fig. 3) the jump in Eshelby tensor gives realistic release rates for the different models.

Model 1 performs well with large elements, even though a small scale phenomenon is introduced in the formulation. Apparently, the energy release rate can be computed sufficiently accurate whether or not this phenomenon is resolved with a sufficiently fine mesh. Because Model 2 does not work well near the free edge, and Model 3 involves elastic parameters which are still somewhat uncertain, Model 1 is to be preferred. Another reason for using Model 1 is that it allows for straightforward application of Zou's method, which will show to be useful for the mode partitioning in Section 3.

2.4. Solid vs. shell formulation

Model 1 involves the stacking of shear deformable plates or shells. Each layer is represented as a 5-parameter shell: a 2D field is defined in the shell mid-surface consisting of three translations and two rotations. In the uncracked part the two layers are connected; 3 of the 10 parameters of the two-layered shell are dependent variables. In a small deformation framework this is easily achieved through elimination of degrees of freedom. In large deformations, however, nonlinear surface ties have to be applied. Especially in large deformations, a more straightforward implementation is possible when a 6-parameter shell is adopted with

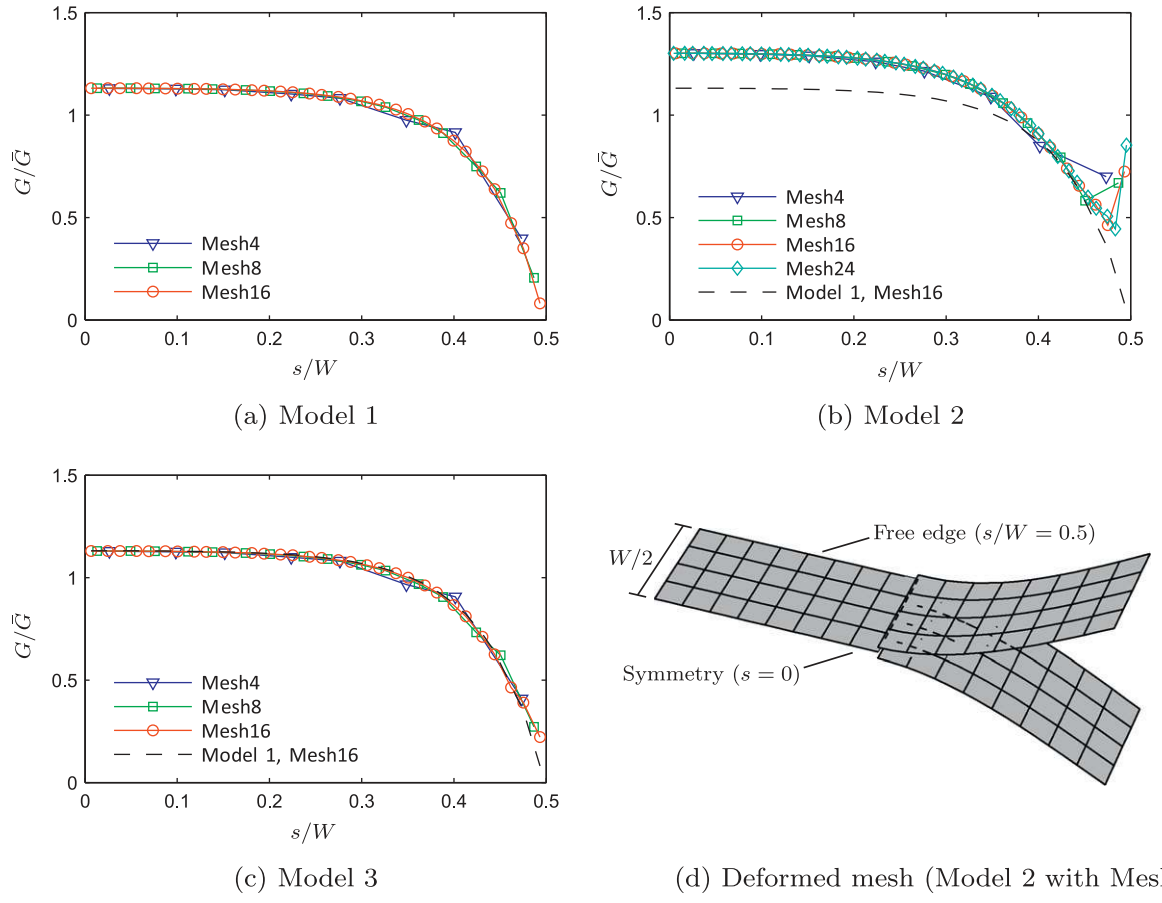

Fig. 4. Convergence of energy release rates along the front of a DCB test for different models. The mesh numbers (4–24) refer to number of elements over the width of the half-specimen. (For interpretation of the references to color in this figure legend, the reader is referred to the web version of this article.)

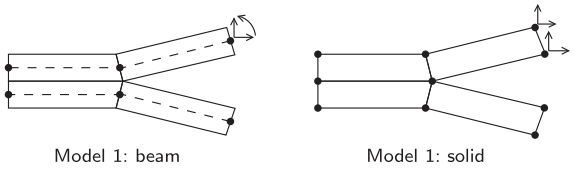

Fig. 5. Beam and solid representation of Model 1 in 2D.

only displacement degrees of freedom.[1] The two different approaches are compared in Fig. 5 for the case of a beam (here it is a 3-parameter extensible Timoshenko beam vs. a 4-parameter 2D solid representation). It is obvious from the figure that the coupling is more straightforward in the solid case, because it is handled through connectivity of the nodes located at top and bottom surfaces.

However, the solid representation is much less robust in terms of the energy release computations in irregular meshes. This is illustrated with a simple example of beam analysis of a double cantilever beam. A finite element mesh of 6-node solid elements (see Fig. 6) or 3-node beam elements is used to model half of a DCB-specimen. The mesh is regular with element length $\Delta x = 4h$, except that one additional element interface is located at a variable location defined by the crack length c. This means that the mesh is irregular around the crack tip, similar to what it would be when the front is moving through an element and modeled with our recent level set model [22]. The material is isotropic. The energy release as computed with the jump in Eshelby tensor is presented in Fig. 6 for different values of the tip location with both solid and beam models. Results are normalized with $\bar{G}$ which is the value

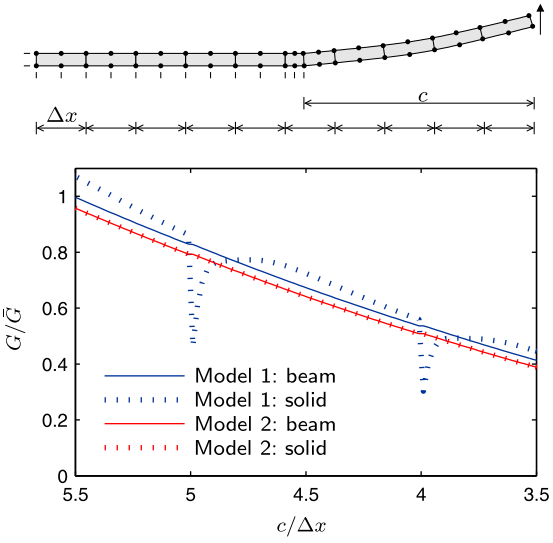

Fig. 6. Energy release rate in DCB test as a function of tip location with crack tip on an additional element boundary in an otherwise regular mesh.

[1] In fact, with nonzero Poisson's ratio, such formulation requires a seventh parameter to avoid Poisson thickness locking, but this one may be condensed out [27,28]. Here we only consider a simple example with $\nu = 0$.

obtained with Model 1 and beam elements for $a/\Delta x = 5.5$. The increase in G as the "crack tip" moves to the left is due to the constant load that is applied on the end and the difference between Models 1 and 2 is again due to the spurious stiffness in Model 2. It is most striking that a big error is observed for Model 1 with solid elements when the crack tip approaches one of the fixed element boundaries.

The inaccuracy for irregular meshes with solid elements is different to what happens with VCCT when elements ahead and behind the crack tip are unequally sized, for which Rybicki and Kanninen have proposed a variation to standard VCCT [4]. In contrast with VCCT the element size is completely absent from the formulation with the jump in Eshelby tensor, which consists only of local stress and deformation quantities. The inaccuracy of the solid elements here is due to inaccuracy in the stress field, particularly in relation to the thickness stretch and the coupling between thickness stretch and transverse shear strain. With a fine mesh, the transverse shear and thickness stretch can be solved accurately; with a regular coarse mesh, inaccuracies in the deformations do not affect the jump in Eshelby tensor; but with a coarse irregular mesh severe inaccuracies appear. This kind of inaccuracy is very harmful for the robustness of the energy release rate computation and therefore a Model 1 approach with solid elements is not advisable. In the following section, a Model 1 formulation with beam/shell elements is further investigated in relation to mixed-mode cracking.

3. Mode partitioning

It is a well-documented fact that the delamination fracture toughness of composites depends on the opening mode [11,12]. Therefore, computation of the energy release rate alone as done in the previous section does not suffice to evaluate Griffith's criterion in Eq. (1). It is also necessary to extract information about the opening from the surrounding field that can be used to relate G_c to experimental measurements. Unfortunately, the expression for the Eshelby tensor cannot be decomposed into three components that can be unambiguously related to the three fundamental modes [29]. Because the expression with the jump in Eshelby tensor can be related to the J-integral, decomposition of the fields in symmetric and antisymmetric parts could be considered, following work on the J-integral [30]. However, this approach is not suitable for generic application to cracking in laminates. It cannot be applied to cracking on bimaterial interfaces, and requires the integration path to be symmetric around the crack plane, which is in the current approach only true when the delamination crack is located at the center plane. With the use of Model 1 from the previous section, however, another method to compute the energy release rate for which such decomposition *is* possible comes within reach, namely the method by Zou et al. [15–17].

3.1. Zou's method

Zou et al. [15–17] have proposed a method which was based on Model 1 with a 5-parameter shell description. They also make use of the jump in strain that appears across the configurational interface. Moreover, they have shown that the jump does not disappear when more elements are used through the thickness. This is obviously only true when shell elements are used, refinement through the thickness with solid elements would lead to the LEFM solution with stress singularity.

There is a distributed force vector acting from one sublaminate to the other along the crack front. The magnitude of the distributed force is equal to the jump in generalized force in top and bottom parts (see Fig. 7)

$$F_z = Q_n^+ - Q_n^- \tag{12}$$

$$F_i = N_{ni}^+ - N_{ni}^-, \quad i = n, s \tag{13}$$

In these equations, and the rest of this section, we still use the $\{n,s,z\}$-frame as defined in Fig. 1, which means that n is normal to the crack front rather than to the crack surface. When this force vector is multiplied with the opening gradient vector, the energy release due to crack growth is obtained and it can immediately be decomposed in three pure mode contributions:

$$G_I = F_z[\![u_{z,n}]\!] \tag{14}$$

$$G_{II} = F_n[\![u_{n,n}]\!] \tag{15}$$

$$G_{III} = F_s[\![u_{s,n}]\!] \tag{16}$$

where $[\![u_{z,n}]\!]$, $[\![u_{n,n}]\!]$ and $[\![u_{s,n}]\!]$ are the differences in displacement gradients right of the top and bottom crack surface at the crack front:

$$[\![u_{j,n}]\!] = u_{j,n}|_{n=0^-,z=0^+} - u_{j,n}|_{n=0^-,z=0^-}, \quad j = z, n, s \tag{17}$$

In general, there may also be distributed moments acting on the crack front. However, Zou et al. [15] have shown from equilibrium considerations that these moments are theoretically equal to zero. Nevertheless, in a discretized system they may be significant while the overall solution is still of acceptable accuracy. In that case, it is better to bring them into the formulation, because the bending moments do contribute to the energy dissipation for the discretized system. For the T_n-term, which is multiplied with a jump in curvature $\phi_{n,n}$, it is clear that it is related to mode I. For the $T_s[\![\phi_{s,n}]\!]$-term, this not so obvious, not in the last place because it is not a primary deformation mode (in the thin-plate limit, this jump in curvature necessarily equal to zero). For completeness, we also ascribe it to mode I. Thus, Eq. (14) is replaced with

$$G_I = F_z[\![u_{z,n}]\!] + T_n[\![\phi_{n,n}]\!] + T_s[\![\phi_{s,n}]\!] \tag{18}$$

Another issue that may affect the performance is related to the transverse shear terms, which receive a special treatment to avoid shear locking. In the thin elements that are used in this paper,the transverse shear deformation and force fields are supposed to be extrapolated from a reduced set of sampling points rather than directly interpolated from the displacement field. It is found that away from the sampling points the direct interpolated rotation field values are more accurate than those obtained from reduced integration. Therefore $u_{z,n}$ is obtained with mixed interpolation:

$$G_I = F_z[\![\gamma_{nz} - \phi_n^{DI}]\!] + T_n[\![\phi_{n,n}]\!] + T_s[\![\phi_{s,n}]\!] \tag{19}$$

where superscript DI is used to indicate that the rotation is computed with direct interpolation of the nodal values.

3.2. Numerical example: DCB

Before several mixed mode cases are treated in detail, Zou's formulation with adaptations is tested on the DCB example from Fig. 4. The mesh-refinement study has been repeated with and without the additional moment and direct interpolation of the rotation field. In Fig. 8 the results are presented for the total G using two different expressions for G_I (for this case it holds $G_{II} = G_{III} = 0$). It can be observed that the energy release rate distribution along the front converges to the same values as in Fig. 4 for both expressions, but that the accuracy of the coarser meshes is much higher with Eq. (19). The gain in performance for large elements will be examined in more detail in the mixed mode examples that follow.

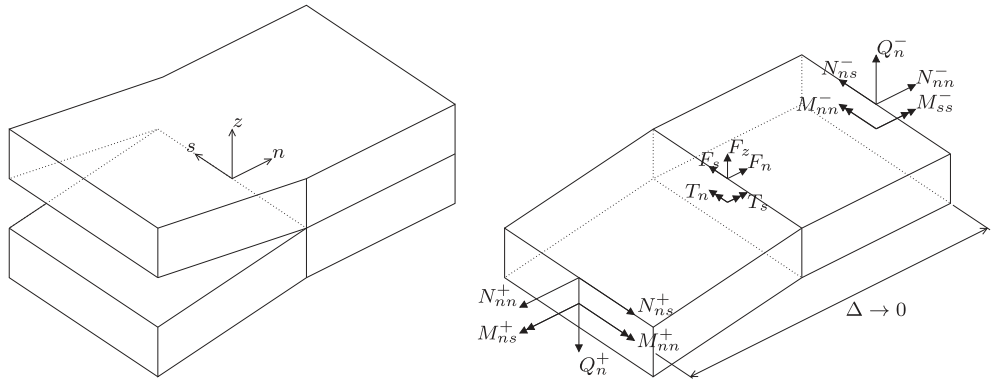

Fig. 7. Definition of force jumps according to Zou et al. [15] on the free body diagram of an infinitesimal extension of the bottom sublaminate around the front.

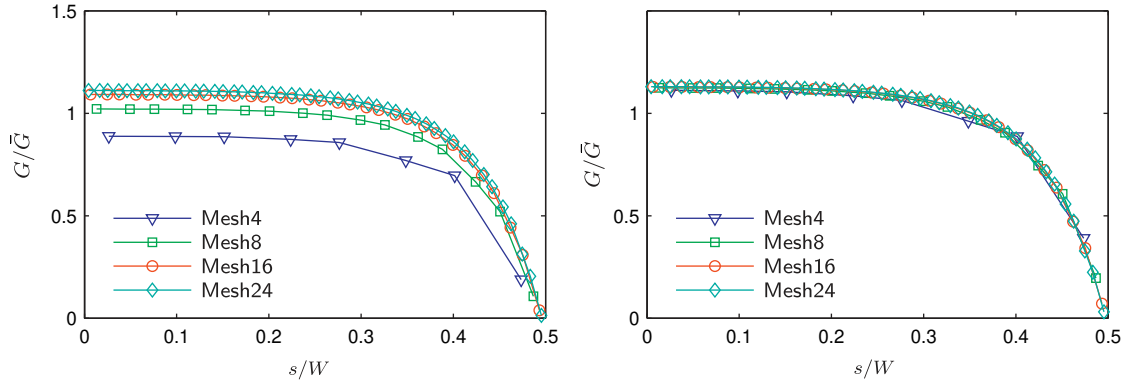

Fig. 8. Mesh-refinement study for energy release rate along the front computed with Zou's method in a DCB test, cf. Fig. 4. (For interpretation of the references to color in this figure legend, the reader is referred to the web version of this article.)

3.3. Review of other methods

Other methods for mode partitioning will also be applied to these examples for comparison. Firstly there are the curvature based relations described by Nilsson and Storåkers [31]. These are very simple, and therefore appealing, but not accurate for even basic cases with unequal arms (with respect to the LEFM solution) and therefore eventually not recommended by Nilsson and Storåkers. But because they possess such attractive simplicity, we include them once more in the comparison. The first relation is based on the idea that equal curvature of the two arms gives a pure mode II case:

$$\frac{K_{II}}{K_I} = \frac{\kappa_B + \kappa_C}{\kappa_B - \kappa_C} \tag{20}$$

The second is based on the idea that opposite curvature weighed with respect to the arm heights gives a pure mode I case:

$$\frac{K_{II}}{K_I} = \frac{h_B\kappa_B + h_C\kappa_C}{h_B\kappa_B - h_C\kappa_C} \tag{21}$$

Notably, for equal arm heights the two criteria are equivalent. These ratios in stress intensity factors K_I and K_{II} are related to ratios in release rate contributions via the standard fracture mechanics relation:

$$\frac{K_{II}^2}{K_I^2} = \frac{G_{II}}{G_I} \tag{22}$$

Then there are the relations by Davidson et al. [18,19] which have been shown to offer a more realistic characterization of the mode mixity in terms of predicting the fracture toughness than LEFM. The basic relation for mixed mode I/II loadings is given as

$$\frac{G_{II}}{G} = \frac{[N_c\sqrt{c_1}\cos\Omega + M_c\sqrt{c_2}\sin(\Omega+\Gamma)]^2}{c_1N_c^2 + c_2M_c^2 + 2\sqrt{c_1c_2}N_cM_c\sin\Gamma} \tag{23}$$

where N_c and M_c depend on the stress state around the front and the thickness and stiffness of the arms. Coefficients Γ, c_1 and c_2 also depend on thickness and stiffness of the arms, while Ω is a phenomenological function of the ratio of arm heights. The expression is based on fracture mechanics considerations, with the exception of the relation for Ω. This relation is optimized to give a good fit with experimental data, i.e. the relation is chosen such that a fixed ratio G_{II}/G corresponds with a constant measured value of G_c for a range of different cases and layups [18]. For the complete relations, the reader is referred to [19].

3.4. Numerical example: MMB

The mixed mode bending (MMB) test is designed as a combination of the pure mode I double cantilever beam and pure mode II end-notched flexure test. With a fixed specimen geometry, the theoretical mode mix is prescribed by changing the ratio of applied loads F_e/F_m (see Fig. 9a). For the MMB test, it has been shown that cohesive methods give the same mode-mix as LEFM [8,32].

As a starting point, we use an analytical solution for a shear deformable beam with Eq. (10) for the deformation of the uncracked part. The mode ratio is computed as:

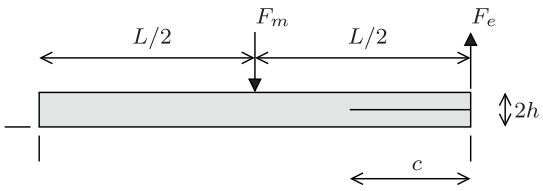

(a) MMB test

(b) Deformed mesh for $\beta^{\text{in}} = 0.8$

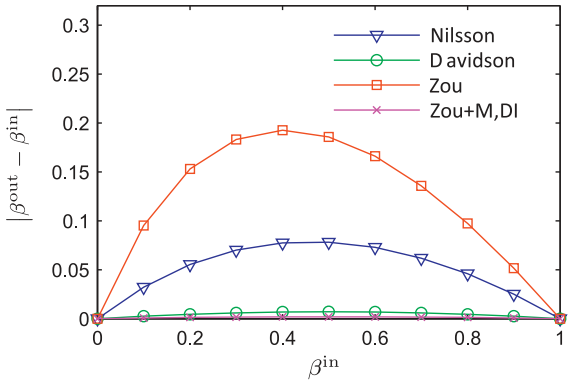

(c) Error plot for $E/\mu = 2$

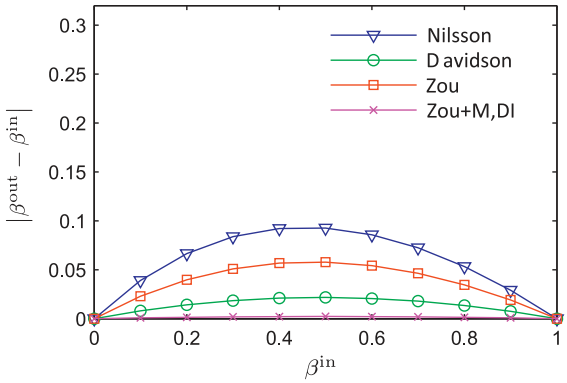

(d) Error plot for $E/\mu = 20$

Fig. 9. Error in predicted mode ratio β^{out} for different values of β^{in} according to Eq. (24). (For interpretation of the references to color in this figure legend, the reader is referred to the web version of this article.)

$$\beta^{\text{in}} = \frac{G_{II}}{G_I + G_{II}} = \frac{\frac{3}{64}F_m^2}{\frac{3}{64}F_m^2 + \left(F_e - \frac{1}{4}F_m\right)^2(1 + 2\lambda + \lambda^2)} \tag{24}$$

with

$$\lambda = \frac{h}{c}\sqrt{\frac{E}{12\alpha\mu}} \tag{25}$$

where c is the crack length, h the height of the beam arms and $\alpha = 5/6$ is Timoshenko's shape coefficient that is also used to reduce the stiffness of the finite elements.

The mixed mode bending test is analyzed for different load pairs F_m/F_e which correspond with different values of the mode mix β^{in} according to Eq. (24). A slenderness ratio c/h of 32 is used and two different ratios between the shear and Young's modulus: $E/\mu = 2$ and $E/\mu = 20$, the former being typical for an isotropic material, the latter for a unidirectional fiber reinforced composite material. Furthermore, a relatively coarse mesh of 3-node shear deformable beam elements with $\Delta x/h = 4$ is used for Zou's method, while the relations by Nilsson and Storåkers [31] and Davidson et al. [19] are applied analytically. The computed mode ratios β^{out} with the different methods are compared with the input values β^{in} in Fig. 9. It can be observed that the simplest formulation based on the curvature of the two arms as proposed by Nilsson and Storåkers is not accurate even for this very basic case. The more advanced formulation by Davidson et al. is very accurate for the beam with high shear stiffness. It is exact for the limit case of very large λ. For the case of relatively small λ however, it is less accurate because shear deformation of the uncracked part does not appear in the formulation. The original formulation by Zou et al. [15] (Eq. (14), denoted Zou) is not accurate for this relatively coarse mesh. However, when the proposed modifications are applied (Eq. (19), denoted ZOU + M,DI) an accurate value is obtained over the whole range for both cases.

The inaccuracy of Zou's original method is due to the use of large elements which is demonstrated with a mesh-refinement study for the case with $\beta^{\text{in}} = 0.4$. In Fig. 10, computed values for pure mode and total energy release rates from different formulas are given for a range of meshes. We use $E/\mu = 2$ which proved to be the more challenging case for Zou's model and element aspect ratios in the range of $0.04 < \Delta x/h < 16$. The energy release rate values are normalized with respect to the analytical total energy release for the given geometry and loads. With $\beta^{\text{in}} = 0.4$ this means that values of 0.4, 0.6 and 1.0 should be obtained for G_{II}, G_I and G, respectively.

It can be observed that G_{II} as computed with Zou's method converges very quickly, while there is a big error in G_I computed with the original version. An element size of $\Delta x = 0.1h$ or smaller is needed to get an accurate prediction for G_I, which is indeed the degree of mesh density Zou et al. use when verifying their method [15]. The adapted relations, however, correct the error for large elements. The largest gain is made when adding the moment terms

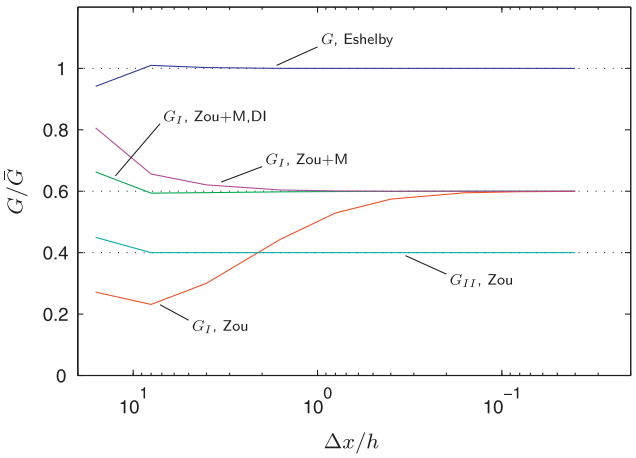

Fig. 10. Mesh-refinement study for energy release rate in MMB test with $\beta^{\text{in}} = 0.4$ and $E/\mu = 2$. (For interpretation of the references to color in this figure legend, the reader is referred to the web version of this article.)

going from Zou with Eq. (14) to Zou + M with Eq. (18). The second modification for Zou + M,DI leads to further improvement such that highly accurate values are obtained for all aspect ratios up to a value of 10. The fact that both Zou and Zou + M converge to the same value for G_I upon mesh refinement confirms that the contribution from the concentrated moment vanishes theoretically.

3.5. Numerical example: UDCB

Next we analyze the case of an unsymmetric double cantilever beam with equal moments, see Fig. 11. For this case a LEFM reference solution is available. With a single material in the specimen, this is still a fairly simple case. Nevertheless, different models do not agree here, as illustrated in Fig. 12, where the phase angle K_{II}/K_I in stress intensities (or $\sqrt{G_{II}/G_I}$) as predicted by different models is shown. Results are shown for linear elastic fracture mechanics following Hutchinson and Suo [33], for the modified fracture mechanics solution by Davidson et al. [19] and for the simple solution by Nilsson and Storåkers. As noted by Nilsson and Storåkers their solution does not follow the LEFM solution. Notably, however, the solution by Davidson et al. differs significantly from the LEFM solution as well, and they have presented experimental evidence that theirs gives a better characterization of the material behavior [19].

Furthermore, results are shown that have been obtained with interface elements and a simple isotropic damage-based cohesive law (see Appendix A for details). The analyses are performed with different values of G_c. The total beam thickness is equal to 3 mm and the fracture toughness G_c is varied from 2 N/mm to 0.002 N/mm. The material is considered isotropic with $E = 100 \times 10^3$ N/mm^2 and $\nu = 0.3$. It is found that the computed mode mix depends significantly on the fracture toughness. For very small fracture toughness the LEFM solution is retrieved, while for relatively high fracture toughness, the mode mix approaches the values predicted by Davidson's method. The variability in cohesive

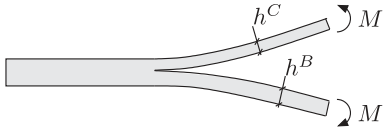

Fig. 11. Unsymmetric double cantilever beam (UDCB).

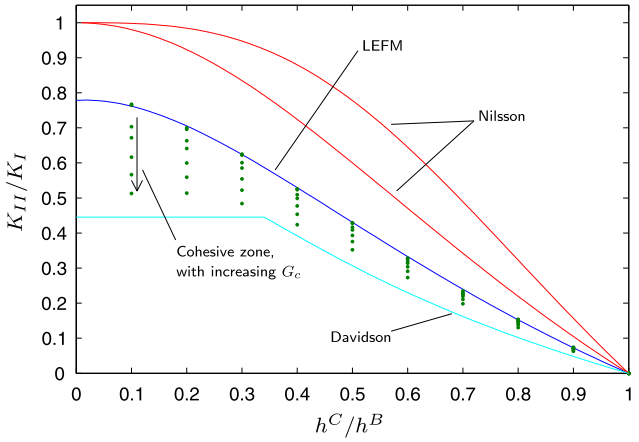

Fig. 12. Mode phase angle from unsymmetric double cantilever beam (UDCB) analysis with different models. (For interpretation of the references to color in this figure legend, the reader is referred to the web version of this article.)

results can alternatively be understood as a size effect, since a similar trend could be obtained by changing the beam thickness while keeping G_c constant.

The difference between mode mix predictions by LEFM and a cohesive method fortifies the question how the mode mix should be characterized. When the two are not equal, this indicates that

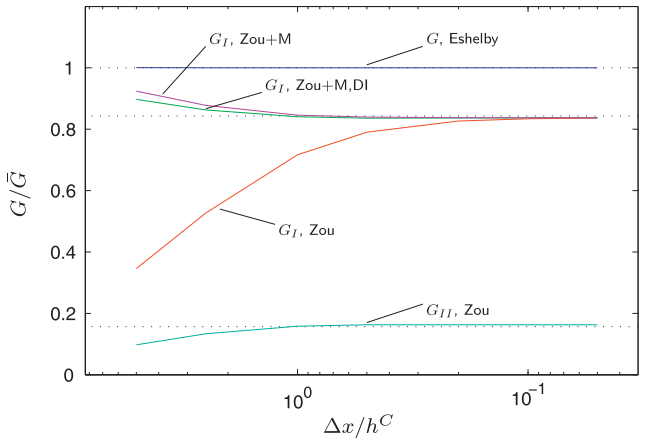

Fig. 13. Mesh-refinement study for energy release rate in UDCB test with $h^C/h^B = 0.5$ and $E/\mu = 2$. (For interpretation of the references to color in this figure legend, the reader is referred to the web version of this article.)

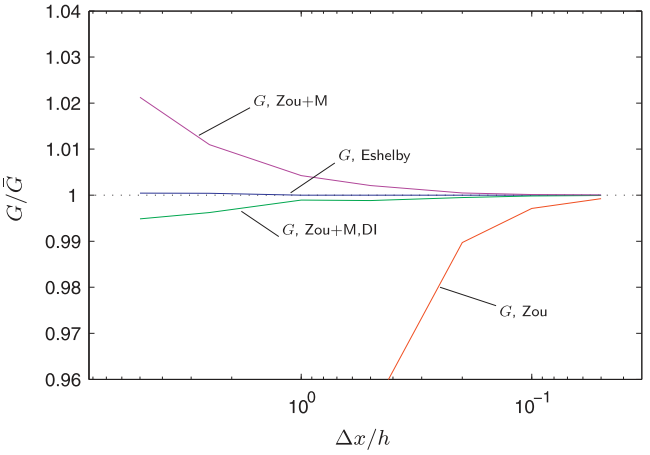

Fig. 14. Total energy release rates in UDCB test computed with different methods (cf. Fig. 13). (For interpretation of the references to color in this figure legend, the reader is referred to the web version of this article.)

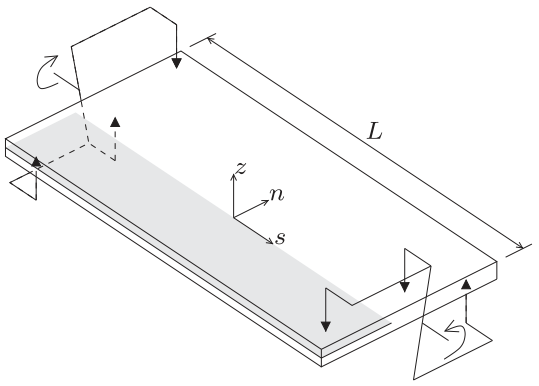

Fig. 15. Six-point edge-cracked torsion test [34].

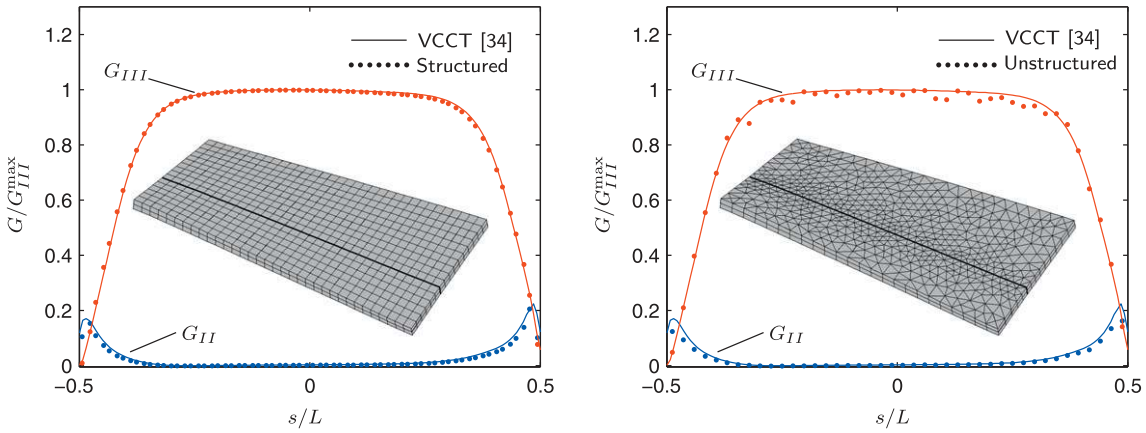

Fig. 16. Energy release rate as computed with Zou's method and a structured and unstructured mesh in comparison with VCCT results by Pereira et al. [34]. (For interpretation of the references to color in this figure legend, the reader is referred to the web version of this article.)

the small-process-zone assumption of fracture mechanics is not valid, which is in line with the experimental observations by Davidson et al. [19]. And indeed the cohesive zone results are not far from those predicted by Davidson's theory. However, the cohesive mode mix does approach the LEFM values when G_c is decreased (or the beam height is increased). This indicates that there is a size effect in the mode mix which is not present in Davidson's relations either. Whether such size effect exists will have to be verified experimentally. In any case, the inconsistency between LEFM and cohesive methods for this simple case demands further research.

Notwithstanding these uncertainties, it is of interest to assess how the proposed method performs for the UDCB case with large elements. For this purpose, a mesh refinement study is performed for the case of $h^C/h^B = 0.5$. Zou et al. [15] have shown their method to converge to the LEFM results only if multiple elements are used through the thickness of both arms. For this case, four and two layers of elements in the thick and thin arms, respectively, were shown to be sufficient. For this through-thickness discretization and a range of element sizes, results are shown in Fig. 13. Again results are normalized with respect to the total energy release rate and dotted lines indicate reference values, derived from the value for K_{II}/K_I from the 2D VCCT analysis reported by Zou et al. [15]. It can be observed that, also in this case, G_{II} converges very quickly, while the results for G_I are much better for large elements when the additional term with the concentrated moment is added (Zou + M). Improvement due to the direct interpolation of rotations (Zou + M,DI) is also still present, but much smaller than before. Altogether, the minimum in-plane mesh size that is needed to obtain high accuracy is approximately an order of magnitude larger when the proposed improvements are applied. This is less than the almost two orders of magnitude improvement in the MMB case, but still considerable.

Fig. 14 presents the total energy release rate computed with different methods in a detailed plot around $G/\overline{G} = 1$. It can be observed that the method with the Eshelby tensor is most accurate for all used discretizations.

The results in Figs. 13 and 14 are for an isotropic material ($E/\mu = 2$). Also in this case much smaller errors (with respect to the LEFM limit) are found with the same discretization when the E/μ ratio is increased.

3.6. Numerical example: 6ECT

Finally, the performance of the method is shown for a more complex case, namely that of the six-point edge cracked torsion test developed by Pereira et al. [34] (see Fig. 15). This setup has been developed for mode III characterization of laminates, but there is a small mode II contribution near the free edges. The case is analyzed with two different coarse discretizations: a structured mesh of 9-node shell elements and an unstructured mesh of 6-node shell elements. Material parameters and geometry are taken from the symmetric laminate described by Pereira et al. [34] and results are compared with VCCT results presented in that same paper (for notch length 30 mm).

In Fig. 16, the used meshes and the obtained energy release rate distributions are shown. The results are in good agreement with each other. Most notably, the discretizations are many times coarser than the VCCT mesh in [34]. Moreover, the fact that similar results are obtained with an unstructured mesh emphasizes the applicability of this method to cases where the crack front has a more complex shapes and/or is evolving. For this coarse discretization, the unstructured mesh gives minor fluctuations in the computed release rate, but these are related to standard inaccuracies in the discretized stress field and therefore they vanish upon mesh refinement.

4. Conclusions

In this paper, different methods for computing the energy release rate for delamination crack growth have been assessed with emphasis on their performance for relatively coarse meshes. It has been shown that as far as computation of the total energy release rate is concerned, the expression with the Eshelby tensor proposed in earlier work [22] gives excellent results, even for very large elements. The accuracy of this technique is compared for three different representations of the uncracked part. Using a single layer of elements in the uncracked part is the most efficient version, but this results in locking near the free edge. The locking can be removed with a rotation spring. Another alternative is to use two layers of elements in the uncracked part. Although this introduces a small-scale phenomenon in the system, it has been shown that large elements can be used for accurate energy release rate computation, provided that an element formulation is adopted which excludes stretching in thickness direction.

With two layers of elements in the uncracked part, another method with which the energy release rate can be computed comes within reach, in which it is possible to partition the release rate into three pure mode rates. This formulation by Zou et al. [15] has been adapted to give better performance for large elements. Particularly the inclusion of concentrated bending moments in

the expression for mode I dissipation improves the accuracy with large elements significantly.

As indicated in the introduction, relations based on the assumption in Eq. (3) do not completely reflect the complexity of the interfacial fracture process. The inconsistency in results that has been shown in this paper from different approaches to the simple UDCB-case, contributes to the uncertainty about the reliability of existing methods. There is need for further research into how the fracture toughness for mixed mode interfacial crack growth is best characterized in a generic sense. The proposed method for mode partitioning is in this respect not different from other methods, but with respect to existing methods it is still commendable for its relaxed mesh-requirements.

In future work with moving crack fronts, the Eshelby tensor and Zou's method can both be used to compute the energy release rate, while Zou's method can furthermore be used to give information on the mode of crack growth. Multiple elements through the thickness are in some cases needed for accurate mode partitioning with Zou's method. But in an adaptive scheme with crack growth, it is possible to use the through-thickness discretization only in a narrow zone around the crack front to further improve efficiency.

Acknowledgments

This work is supported by the Technology Foundation STW (under Grant 06623) and the Ministry of Public Works and Water Management, The Netherlands.

Appendix A. Element formulations

Different element formulations have been used in the numerical examples, in each case with special care to avoid shear locking because thin elements are used. In this appendix, a brief overview of the different elements is given, with references to literature where more details can be found. The computation of the energy release rates is in all cases performed in a post-processing step with the displacement field from linear finite element analysis.

For shell analysis (in Sections 2.3, 3.2 and 3.6) the concept of mixed interpolation of tensorial components (MITC), first proposed for bilinear quadrilateral elements by Dvorkin and Bathe [35], is used. Quadratic elements are used, following the interpolation schemes for 9-node quadrilaterals and 6-node triangles given by Lee and Bathe [36]. However, assumed strains are not used for the in-plane stress components, because curved structures are not considered. In contrast with the original formulation by Bathe and coworkers, the elements are formulated in small displacements, following Alfano et al. [25]. The elements contain five degrees of freedom per node: three translations and two rotations.

In Sections 2.4, 3.4 and 3.5, 3-node beam elements are used. These are extensible shear-deformable beam elements without torsion, which means that there are three degrees of freedom per node: two translations and one rotation. Details of the formulation of such elements can be found in finite element textbooks, e.g. Hughes [37]. Shear locking is avoided with uniform reduced integration, which means that for the quadratic element two integration points are used [37].

In Section 2.4, a comparison is made between solid and beam elements. For this comparison, a solid element is used that is closely related to the 3-node beam element: a 6-node quadrilateral element with quadratic interpolation in length direction and linear interpolation through the thickness. For this element, shear locking is avoided with selective reduced integration [37]: the shear strain contribution is evaluated with a 2×1 integration, while full 3×2 integration is used for the other contributions.

Finally, in Section 3.5, brief reference is made to cohesive zone analyses. In those analysis, a fine mesh of 4-node quadrilateral solid elements with selective reduced integration is used and the interface is modeled with cohesive elements with damage law as described by Turon et al. [8]. The interface is made isotropic by setting $G_{Ic} = G_{IIc}$ to make the results better reproducable and less dependent on the specific cohesive law. These are the only nonlinear analyses performed for this paper. The local mode ratio is computed with pure mode release rates that are obtained through integration of the cohesive law during the analysis: $G_I = \int t_z \, \mathrm{d}[\![u_z]\!]$, $G_{II} = \int t_x \, \mathrm{d}[\![u_x]\!]$. The plotted mode ratio is the average of the local mode ratio over a length that is larger than the size of the cohesive zone.

References

[1] Griffith AA. The phenomena of rupture and flow in solids. Philos Trans Roy Soc Lond, Ser A 1921;221:163–98.
[2] Irwin GR. Analysis of stresses and strains near the end of a crack transversing a plate. J Appl Mech 1957;24:361–6.
[3] Rice JR. A path independent integral and the approximate analysis of strain concentration by notches and cracks. J Appl Mech 1968;35:379–86.
[4] Rybicki EF, Kanninen MF. A finite element calculation of stress intensity factors by a modified crack closure integral. Eng Fract Mech 1977;9(4):931–8.
[5] Krueger R. Virtual crack closure technique: history, approach, and applications. Appl Mech Rev 2004;57(2):109–43.
[6] Yang QD, Cox BN. Cohesive models for damage evolution in laminated composites. Int J Fract 2005;133(2):107–37.
[7] Li S, Reid SR, Zou Z. Modelling damage of multiple delaminations and transverse matrix cracking in laminated composites due to low velocity lateral impact. Compos Sci Technol 2006;66(6):827–36.
[8] Turon A, Camanho PP, Costa J, Dávila CG. A damage model for the simulation of delamination in advanced composites under variable-mode loading. Mech Mater 2006;38(11):1072–89.
[9] Jiang W-G, Hallett SR, Green BG, Wisnom MR. A concise interface constitutive law for analysis of delamination and splitting in composite materials and its application to scaled notched tensile specimens. Int J Numer Method Eng 2007;69(9):1982–95.
[10] van der Meer FP, Sluys LJ. Mesh-independent modeling of both distributed and discrete matrix cracking in interaction with delamination. Eng Fract Mech 2010;77(4):719–35.
[11] Evans AG, Rühle M, Dalgleish BJ, Charalambides PG. The fracture energy of bimaterial interfaces. Mater Sci Eng A 1990;126(1-2):53–64.
[12] Benzeggagh ML, Kenane M. Measurement of mixed-mode delamination fracture toughness of unidirectional glass/epoxy composites with mixed mode bending apparatus. Compos Sci Technol 1996;56(4):439–49.
[13] Wang T-C, Shih CF, Suo Z. Crack extension and kinking in laminates and bicrystals. Int J Solids Struct 1992;29(3):327–44.
[14] Raju IS, Crews Jr JH, Aminpour MA. Convergence of strain energy release rate components for edge-delaminated composite laminates. Eng Fract Mech 1988;30(3):383–96.
[15] Zou Z, Reid SR, Soden PD, Li S. Mode separation of energy release rate for delamination in composite laminates using sublaminates. Int J Solids Struct 2001;38(15):2597–613.
[16] Zou Z, Reid SR, Li S, Soden PD. General expressions for energy-release rates for delamination in composite laminates. Proc Roy Soc Lond, Ser A 2002;458(2019):645–67.
[17] Zou Z, Reid SR, Li S, Soden PD. Application of a delamination model to laminated composite structures. Compos Struct 2002;56(4):375–89.
[18] Davidson BD, Fariello PL, Hudson RC, Sundararaman V. Accuracy assessment of the singular-field-based mode-mix decomposition procedure for the prediction of delamination. In: Hooper SJ, editor. Composite materials: testing and design, vol. 13. ASTM STP 1242, Philadelphia; 1997. p. 109–28.
[19] Davidson BD, Gharibian SJ, Yu L. Evaluation of energy release rate-based approaches for predicting delamination growth in laminated composites. Int J Fract 2000;105(4):343–65.
[20] Wisnom MR. On the increase in fracture energy with thickness in delamination of unidirectional glass fibre–epoxy with cut central plies. J Reinf Plast Compos 1992;11(8):897–909.
[21] Greenhalgh ES, Rogers C, Robinson P. Fractographic observations on delamination growth and the subsequent migration through the laminate. Compos Sci Technol 2009;69(14):2345–51.
[22] van der Meer FP, Moës N, Sluys LJ. A level set model for delamination – modeling crack growth without cohesive zone or stress singularity. Eng Fract Mech 2012;79:191–212.
[23] Ousset Y. Numerical simulation of delamination growth in layered composite plates. Eur J Mech Solids 1999;18:291–312.
[24] Kanninen MF. An augmented double cantilever beam model for studying crack propagation and arrest. Int J Fract 1973;9(1):83–92.
[25] Alfano G, Auricchio F, Rosati L, Sacco E. MITC finite elements for laminated composite plates. Int J Numer Method Eng 2001;50(3):707–38.

[26] Davidson BD. An analytical investigation of delamination front curvature in double cantilever beam specimens. J Compos Mater 1990;24(11): 1124–37.
[27] Büchter N, Ramm E, Roehl D. Three-dimensional extension of non-linear shell formulation based on the enhanced assumed strain concept. Int J Numer Method Eng 1994;37(15):2551–68.
[28] Parisch H. A continuum-based shell theory for non-linear applications. Int J Numer Method Eng 1995;38:1855–83.
[29] van der Meer FP, Moës N, Sluys LJ. A level set approach to delamination – modeling crack growth without cohesive zone or stress singularity. In: Rolfes R et al., editor. Proceedings of 3rd ECCOMAS thematic conference on the mechanical response of composites, Hannover, Germany, September 2011.
[30] Huber O, Nickel J, Kuhn G. On the decomposition of the *J*-integral for 3D crack problems. Int J Fract 1993;64(4):339–48.
[31] Nilsson K-F, Storåkers B. On interface crack growth in composite plates. J Appl Mech 1992;59(3):530–8.
[32] van der Meer FP, Sluys LJ. A phantom node formulation with mixed mode cohesive law for splitting in laminates. Int J Fract 2009;158(2):107–24.
[33] Hutchinson JW, Suo Z. Mixed mode cracking in layered materials. Adv Appl Mech 1992;29:63–191.
[34] Pereira AB, de Morais AB, de Moura MFSF. Design and analysis of a new six-point edge crack torsion (6ECT) specimen for mode III interlaminate fracture characterization. Composites Part A 2011;42(2):131–9.
[35] Dvorkin EN, Bathe KJ. A continuum mechanics based four-node shell element for general non-linear analysis. Eng Comput 1984;1:77–88.
[36] Lee P-S, Bathe KJ. The quadratic MITC plate and MITC shell elements in plate bending. Adv Eng Softw 2010;41(5):712–28.
[37] Hughes TJR. The finite element method: linear static and dynamic finite element analysis. Englewood Cliffs (NJ): Prentice-Hall; 1987.